Internal tide dissipation, mixing, and vertical nitrate flux at the shelf edge of NE New Zealand

Jonathan Sharples and C. Mark Moore

Southampton Oceanography Centre, Empress Dock, Southampton, England, United Kingdom

Edward R. Abraham

National Institute of Water and Atmospheric Research, Greta Point, Kilbirnie, Wellington, New Zealand

Abstract. An internal tide on the NE shelf of New Zealand was observed with a combination of moored temperature loggers and current meters and vertical profiling with a microstructure probe. Internal tide energy flux across the shelf edge was calculated to be ~400 W m^{-1}, with considerable variability driven by the passage of a storm through the region. Energy associated with the internal tide was significantly greater than the energy of the barotropic tide or of inertial shear. Dissipation of the internal tide calculated from the energy loss between two of the moorings was estimated to be 15 ± 10 mW m^{-2}. The associated vertical eddy diffusivity was (4 ± 3) × 10^{-4} m^2 s^{-1}. The microstructure observations indicated internal tide–driven vertical diffusivities at the nitracline of ~7 × 10^{-4} m^2 s^{-1}. The observations of vertical eddy diffusivities are combined with measurements of the vertical nitrate gradient to suggest that mixing driven by the internal tide is the dominant mechanism for driving diapycnal nutrient supply during summer. The calculated flux of about 12 mmol N m^{-2} d^{-1} into the photic zone is suggested to drive significant new subsurface production throughout the summer, amounting to a possible contribution to annual new production on the shelf of 100 g C m^{-2}.

1. Introduction

Shelf slope and adjacent shelf sea regions have been recognized for some time as areas influenced by internal tides [e.g., *Huthnance*, 1989]. Interaction between the barotropic tidal flow and the bathymetry of the shelf break and slope region causes vertical perturbations of the water column density structure, which then propagate both on- and off-shelf as tidal period internal waves. The link between observations of such waves and the theory of their propagation and structure is now well established [e.g., *Baines*, 1982; *Gerkema*, 1996]. Attention has also focused on the dissipation of these waves and the associated internal mixing. In shelf regions this internal mixing has been suggested to play a key role in shelf edge primary production by providing a mechanism for mixing nutrients across the pycnocline [*Holligan et al.*, 1985]. At the shelf slope and within the ocean interior this topographically driven tidal baroclinic mixing is now believed to be important in ventilating the deep ocean [*Sjöberg and Stigebrandt*, 1992; *Munk and Wunsch*, 1998; *Ledwell et al.*, 2000]. Quantifying both the global geographical distribution of internal mixing, and determining the effects of this mixing on the physical, chemical, and biological structure of the water column, is a key area of research in oceanography.

Assuming shelf sea barotropic tidal currents u between 0.1 and 1 m s^{-1}, the dissipation rate of barotropic tidal energy ranges between 3 × 10^{-3} and 3 W m^{-2} (using tidal dissipation = $k_b \rho u^3$, with k_b = 0.003 and ρ the density of seawater [*Simpson and Bowers*, 1981]). Observations of the dissipation rate of baroclinic tidal energy in shelf seas typically range

between 10^{-3} and 10^{-2} W m^{-2} [e.g., *Holloway*, 1984; *Sherwin*, 1988; *Largier*, 1994]. Thus the energy dissipation by baroclinic tides is generally at the lower end of the range typical for barotropic currents. However, the importance of baroclinic energy dissipation lies with where in the water column the energy is dissipated. Barotropic tidal energy is dissipated in the tidal boundary layer, so that the effective efficiency of this mixing acting on the near-surface density structure of the water column is <1% [*Simpson and Bowers*, 1981]. Baroclinic energy is dissipated on the density structure that supports the internal wave, and so, the efficiency of this turbulent mixing in raising the potential energy of the water column is higher. The internal tide transfers barotropic tidal energy (at the shelf slope) into a form more conducive to diapycnal transfer.

Most observational estimates of the mixing associated with the passage and decay of an internal wave have used moored thermistors. The potential energy of the wave can be calculated from the vertical displacements inferred from a time series of temperature profiles, and the kinetic energy is often calculated using a result from linear theory:

$$\frac{\text{PE}}{\text{KE}} = \frac{(\omega^2 - f^2)}{(\omega^2 + f^2)}, \quad (1)$$

where ω is the tidal frequency and f is the Coriolis parameter [*Fofonoff*, 1969]. A similar time series of vertical profiles of current speed could, of course, lead directly to an estimate of the internal wave kinetic energy, and such combined observations of current velocities and thermal structure have been shown to support (1) [*Sherwin*, 1988]. The energy dissipation rate ε is then simply the difference between the energies observed at two moorings divided by the wave propagation time between them. If the vertical distributions of dissipation and

buoyancy frequency (N^2 s^{-2}) are similar, then an estimate can be made of the associated vertical eddy diffusivity K_ρ via

$$K_\rho \approx \Gamma \, \frac{\varepsilon}{N^2} \qquad \text{m}^2\,\text{s}^{-1} \qquad (2)$$

[*Osborn*, 1980]. The factor Γ is parameterized by the flux Richardson number R_f, by $\Gamma = R_f/(1 - R_f)$. Here we use the usual constant value of $\Gamma = 0.2$ [e.g., *Moum*, 1996]. Using this approach, vertical diffusivities attributable to internal tides have been estimated on the NW Australian shelf to be 1.4 × 10^{-4} m^2 s^{-1} [*Holloway*, 1984] and on the South African shelf to be 1.1 × 10^{-4} m^2 s^{-1} [*Largier*, 1994].

An alternative method of quantifying internal turbulent dissipation is to use free-fall microstructure instruments, measuring either velocity or temperature gradient microstructure. Such instruments have been used extensively in the ocean [e.g., *Gregg*, 1998] and in lakes [e.g., *Imberger and Ivey*, 1991]. Direct microstructure-based estimates of mixing in shelf seas by the internal tide are so far limited. *Sandstrom and Oakey* [1995] calculated mean vertical diffusivities of between 10^{-5} and 10^{-4} m^2 s^{-1} associated with the internal tide on the Scotian shelf. *Inall et al.* [2000] have recorded mean dissipation rates of the internal tide on the Malin shelf of 1.1 × 10^{-2} (neap tides) and 4.0 × 10^{-2} W m^{-2} (spring tides), driving vertical diffusivities of 5 × 10^{-4} and 1.2 × 10^{-3} m^2 s^{-1}, respectively.

In this paper we present time series of vertical temperature and current profiles from an array of moorings on the NE New Zealand shelf, along with profiles of vertical diffusivities acquired with a free-fall temperature gradient microstructure profiler. Analysis of the mooring observations illustrates the variability of the baroclinic energy associated with the internal tide and with inertial oscillations, including the destruction and subsequent recovery of the internal tide caused by the passage of a storm. During a period of the deployment dominated by internal tidal energy an estimate of the mean vertical diffusivity is made using the dissipation of the internal tidal wave between two moorings on the shelf. Tidally averaged estimates of dissipation profiles measured with the microstructure profiler show the vertical profiles of diffusivities at the nitracline associated with the internal tide. The dissipation and nitrate gradient allow an estimate of the vertical nitrate flux driven by the internal tide into the photic zone. We discuss this nutrient flux in terms of the potential for new primary production during summer on the NE New Zealand shelf.

2. Method

2.1. Moorings

Five moorings were deployed on the shelf and upper slope of NE New Zealand between November 25, and December 8, 1998 (Figure 1a). The orientation of the mooring array was designed to lie along the propagation direction of a shoreward moving internal tidal wave, as shown by available synthetic aperture radar (SAR) imagery (Figure 1b). The location of the moorings is shown along with the cross-shelf bathymetry of the region (Figures 1a and 1c). The instrumentation, sampling rates, and data quality for each mooring are summarized in Table 1. All times are presented as New Zealand Standard Time (NZST = UT + 12 hours).

Moorings IW2 (shelf edge) and IW4 (midshelf) were the most heavily instrumented. The aim was to use the temperature logger information to provide estimates of the amplitude,
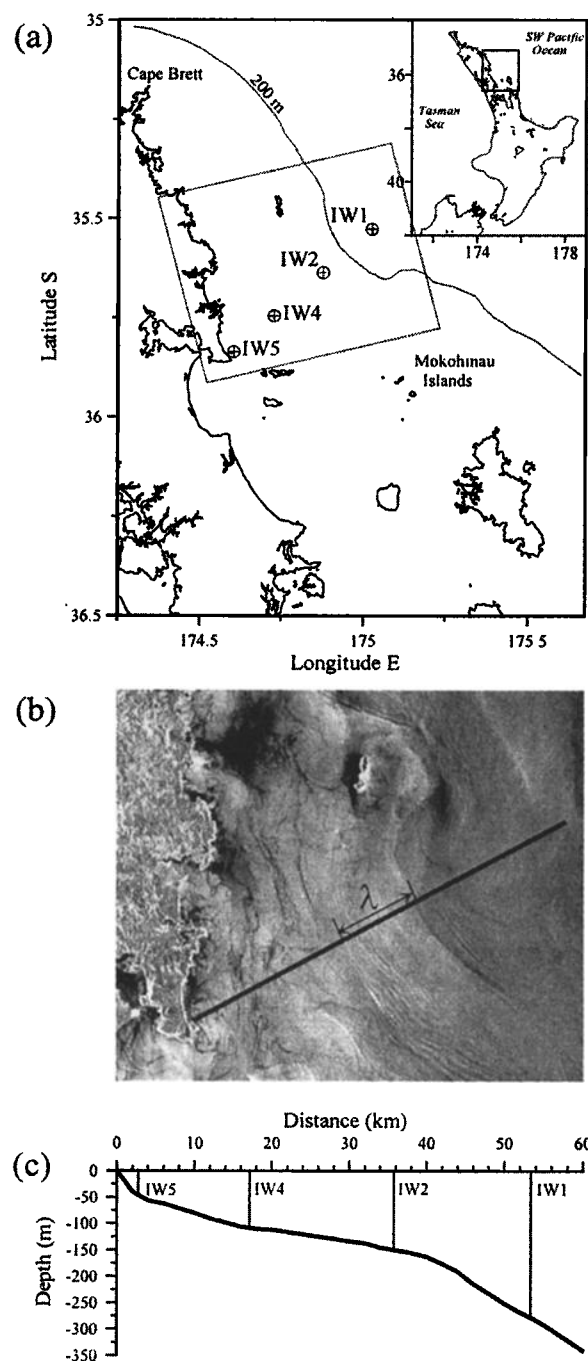

Figure 1. (a) Positions of the moorings on the NE shelf of North Island, New Zealand. Wind speed observations were taken from a weather station on the Mokohinau Islands. (b) ERS-1 SAR image of the boxed region in Figure 1a, taken on November 17, 1995. Two internal tidal wave fronts can be seen, each associated with a number of short-wavelength internal waves. The internal tide wavelength λ is ~15 km. The bold line marks the orientation of the mooring array. Image data are courtesy of the European Space Agency. (c) Positions of the moorings relative to the cross-shelf bathymetry.

and therefore potential energy, of the internal tide. The current profiles from the acoustic Doppler profilers (ADPs) and Aanderaa recording current meters RCMs could then be used to calculate the kinetic energy of the internal tide, thus result-

Table 1. Details of the Mooring Array in Figure 1[a]

Mooring	Position	Depth, m	Instrumentation	Sampling Rate	Remarks
IW1	35°31.68'S, 175°01.39'E	300	RCM: 15, 100, 200, 240, 280 mab	5 min	good data
IW2	35°38.22'S, 174°52.59'E	150	RCM: 10, 20, 30 mab	5 min	no temperature from RCM at 10 mab
			H: 2, 50, 60, 70, 80, 90, 100, 110, 120, 130, 140 mab	1 min	good data
			ADP: 40 mab	1 min 5 m bins	temperature good, no useful currents
			NAS2: 125 mab	30 min	good data
IW4	35°44.76'S, 174°43.59'E	110	H: 10, 20, 30, 40, 50, 60, 70, 80, 90, 100 mab	1 min	good data
			ADP: 5 mab	1 min 5 m bins	good data
IW5	35°50.20'S, 174°36.20'E	30	H: 15 mab	1 min	good data

[a]RCM, Aanderaa RCM 7; H, Hungren temperature logger; ADP, Sontek 500 kHz acoustic Doppler profiler; and NAS2, WS Ocean Systems nitrate analyzer. Instrument positions are all meters above bed (mab).

ing in the total wave energy at the two sites. However, the ADP on mooring IW2 did not return any valid current measurements, which prevented direct calculation of kinetic energy at this site. The only other instrument problem was a failure of the temperature sensor on the RCM 10 m above the bed (mab) on IW2. Given that the temperature records at 2, 20, and 30 mab showed that the water column was always well mixed to at least a height of 20 m, this was not a serious limitation to the analysis. Mooring IW2 also had a WS Ocean Systems NAS2 nitrate analyser situated 25 m below the sea surface in order to observe changes in the near-surface nitrate concentration driven by the oscillation of the internal tide.

Hourly 10 min averages of wind speed and direction were taken from an automatic weather station on the Mokohinau Islands (Figure 1a). Eastward and northward components of wind stress (τ_x and τ_y (N m^{-2})) were then calculated using

$$\tau_x = c_d \rho_a \sqrt{(u_w^2 + v_w^2)} \, u_w \qquad (3a)$$

$$\tau_y = c_d \rho_a \sqrt{(u_w^2 + v_w^2)} \, v_w, \qquad (3b)$$

with $\rho_a = 1.3$ kg m^{-3} the density of air and u_w and v_w (m s^{-1}) the eastward and northward components of wind speed. The surface drag coefficient c_d was related to wind speed w (m s^{-1}) with [Garratt, 1977]

$$c_d = (0.75 + 0.067w) \times 10^{-3}. \qquad (4)$$

2.2. Conductivity-Temperature-Depth

Four conductivity-temperature-depth (CTD) and microstructure stations, each lasting approximately one tidal cycle, were occupied during the latter part of the mooring deployment, two by mooring IW4 (December 2 and December 7) and two by mooring IW2 (December 5 and December 6). A Seabird 911 CTD was used to collect salinity and temperature profiles; discrete salinity samples were collected and later analyzed on a Guildline Autosal, calibrating the salinity data to ±0.005 (using the Practical Salinity Scale 1978). Water samples were taken from the CTD rosette for nitrate and chlorophyll analysis. Nitrate samples were filtered (Whatman GF/F) and frozen for later analysis following the method detailed by Strickland and Parsons [1968]. Chlorophyll samples were filtered onto Whatman GF/F filters, and then extracted for 4

hours in 90% acetone in a refrigerator. The supernatant was read on a spectrofluorometer before and after acidification.

A free-falling Self-Contained Autonomous Microstructure Profiler (SCAMP) was used to measure the vertical temperature gradient microstructure. The vertical diffusivity of heat, K_T, and the turbulent dissipation rate can both be calculated from adequately resolved temperature microstructure. If it is assumed that the vertical flux of thermal variance dominates lateral fluxes, as will be the case where vertical temperature gradients are much greater than lateral gradients, then the vertical diffusivity of heat can be written [Osborn and Cox, 1972]

$$K_T = \frac{\chi}{2} \left(\frac{\partial \overline{T}}{\partial z} \right)^{-2} \qquad \text{m}^2 \text{ s}^{-1}, \qquad (5)$$

with ($\partial \overline{T}/\partial z$) the vertical gradient of the mean temperature structure. Assuming isotropic turbulence, the rate of dissipation of thermal variance χ is estimated from

$$\chi \approx 6D_t \overline{\left(\frac{\partial T}{\partial z} \right)^2} \qquad °\text{C}^2 \text{ s}^{-1}, \qquad (6)$$

with D_t the molecular diffusivity of heat (1.4 × 10^{-7} m^2 s^{-1}). The turbulent dissipation can be estimated from [Oakey, 1982]

$$\varepsilon = k_B^4 \nu D_t^2 \qquad \text{m}^2 \text{ s}^{-3}, \qquad (7)$$

with ν the molecular viscosity (1.4 × 10^{-6} m^2 s^{-1}) and k_B is the Batchelor wavenumber, calculated by fitting a Batchelor spectrum to the observed temperature gradient spectrum [Ruddick et al., 2000]. The dissipation range measurable by SCAMP is $10^{-10} < \varepsilon < 10^{-5}$ m^2 s^{-3}.

The use of (5), (6), and (7) requires that the temperature gradient microstructure be resolved at the smallest scales ($O(1$ mm)), accomplished with SCAMP using fast response thermistors (Thermometrics FP07s). Because of the intermittent nature of turbulent events, a large number of these profiles needs to be collected in order to obtain statistically robust estimates of χ and k_B and hence of K_T and ε. Because of the slow fall speed (~10 cm s^{-1}) required to resolve adequately the full temperature gradient spectrum, this can impose practical limitations on the use of this method. Typically, each
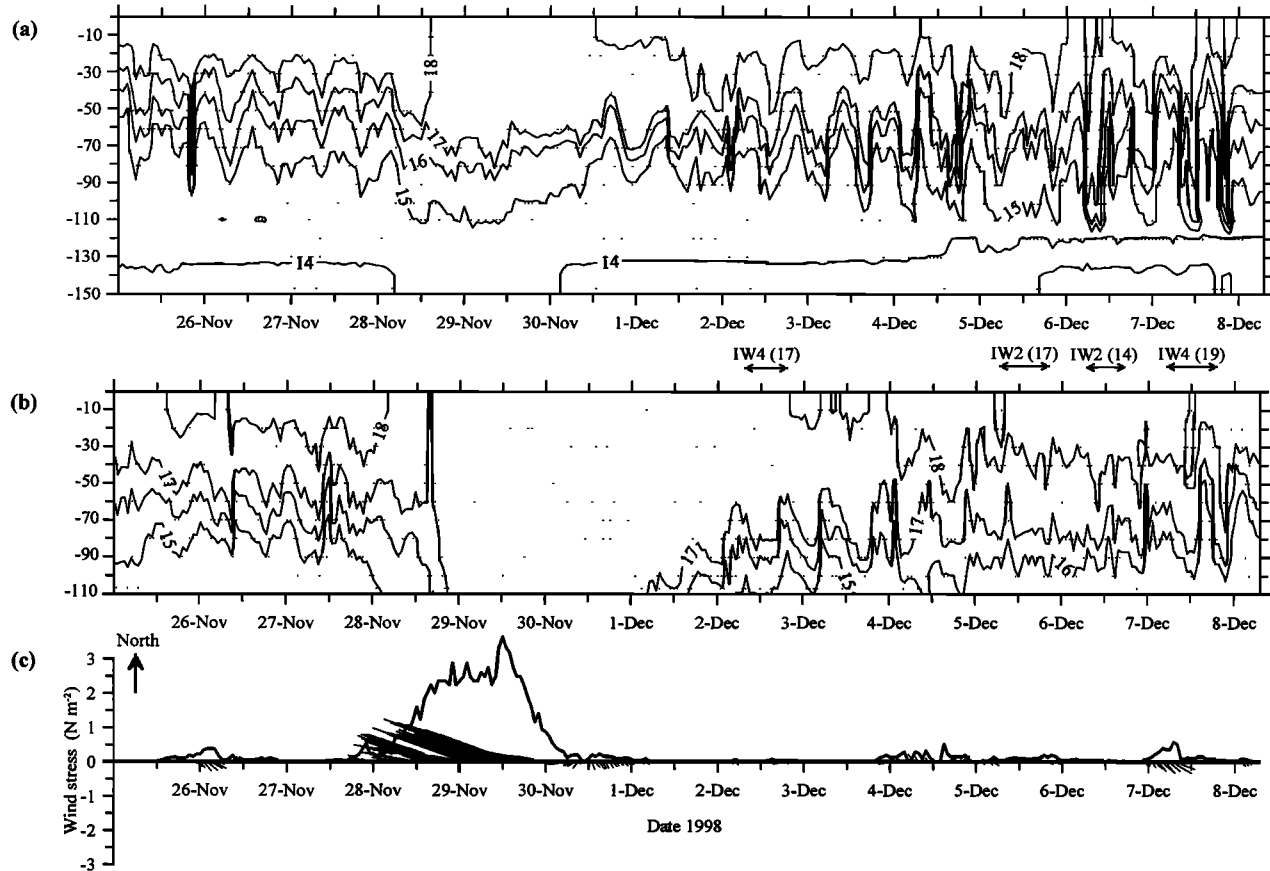
Figure 2. (a) Time series of the vertical temperature structure at mooring IW2, contoured at 1°C intervals. (b) As in Figure 2a but for mooring IW4. (c) Wind stress magnitude and stress vectors during the mooring deployment. The scale for the vectors is the same as the y axis scale. The dotted lines in Figures 2a and 2b indicate the positions of the temperature sensors. The horizontal arrows above Figure 2b indicate the times and positions of the microstructure stations, with the numbers in parentheses showing the total number of SCAMP profiles collected at the station.

70–80 min involved one profile with the CTD and two consecutive profiles with SCAMP. Between 14 and 19 SCAMP profiles were collected at each station. SCAMP has a maximum rated pressure capability of 100 m. However, as the instrument free falls attached to a light tether, the maximum depth of the profiles was generally limited by the drift of the ship and the 200 m length of the tether. Most profiles reached depths of ~70–75 m. The statistical constraints on the turbulence data mean that a single average profile of dissipation and turbulent diffusivity could then be calculated for each station; there were insufficient profiles to allow reliable resolution of the variability of mixing within a tidal cycle. Uncertainties in these time-averaged profiles of dissipation were calculated as 95% confidence intervals using a bootstrap technique [*Efron and Gong*, 1983].

3. Results

3.1. Moorings

The internal tide is generated at the position where the seabed slope is the same as the internal tidal wave characteristic slope c calculated from

$$c = \left(\frac{\omega^2 - f^2}{N^2 - \omega^2} \right)^{1/2}, \tag{8}$$

with ω (s^{-1}) the tidal frequency, f (s^{-1}) the Coriolis frequency at 36°S, and N (s^{-1}) the buoyancy frequency. Using typical observations of the density structure below the depth of the seasonal thermocline, the wave characteristic slope is estimated to be 0.03. In this part of New Zealand the seabed slope reaches this value ~40 km seaward of mooring IW1 in a depth of between 600 and 700 m.

Combining all the temperature time series from moorings IW2 and IW4 provides a detailed picture of the variability in vertical structure at these two sites (Figure 2). Both time series indicate semidiurnal variability in the water column thermal structure. Mid–water column amplitudes of the internal tide at station IW2 were typically 10 m near the beginning of the deployment, increasing to over 35 m towards the end. Amplitudes at IW4 were typically about 10–20 m. A strong downwelling favourable storm that passed through the region on November 28 and 29 had a profound effect on the internal tide. At IW4 the water column was completely mixed within 24 hours of the onset of the storm, eradicating any possibility of internal waves presumably over a large area of the shelf. Following the storm, weak near-surface stratification was slowly reestablished, though the internal tide appeared earlier with near-bed restratification caused by an intrusion of dense bot-
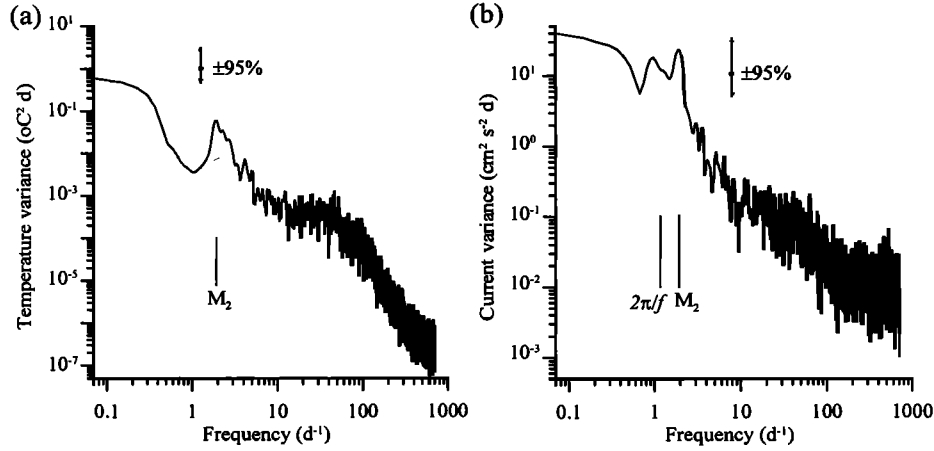
Figure 3. (a) Variance in the temperature record from a depth of 60 m on mooring IW4. (b) Variance of the cross-shelf baroclinic currents 20 m below the surface at mooring IW4. The spectra were averaged with a cosine bell filter, with 10 degrees of freedom.

tom water. At IW2 the initial surface mixed layer of about 30 m mean thickness was deepened rapidly to about 60–70 m, with a weak signature of the internal tide being confined to the lower half of the water column. Again, both near-surface stratification and the reintroduction of colder bottom water occurred as the winds decreased.

The power spectrum of a mid–water column temperature time series from IW4 (Figure 3a) illustrates the dominance of a semidiurnal periodicity in the observations. Horizontal temperature gradients in the vicinity of the moorings were very weak (typically <0.01°C km^{-1}), so this semidiurnal temperature variance was being driven by vertical oscillations associated with an internal tide. Figure 3a also shows considerable higher-frequency variability in the time series, with a broad signal between periods of about 10 and 40 min. These shorter-period internal waves are clearly visible in the SAR image of Figure 1b.

To assess the variability in the baroclinic current the depth mean current was removed from the individual vertical bins in the ADP time series prior to power spectrum analysis. The results (Figure 3b) indicate strong semidiurnal signal in the baroclinic flow, along with significant variability at M_4 and a broad peak, just significant with 95% confidence, centered on a period of 30 min. The power spectrum also shows potentially important variance at the inertial frequency, with a significant peak at a period of $2\pi/f$.

The pattern of variability in the baroclinic currents suggests the steepening and breaking of the internal tidal wave as it passed the mooring, with additional input associated with vertical shear of inertial oscillations. The vertical current shear observed by the ADP on mooring IW4 was calculated by

$$\text{shear}^2 = \overline{\left(\frac{\partial u}{\partial z}\right)^2} + \overline{\left(\frac{\partial v}{\partial z}\right)^2}, \tag{9}$$

with u and v the eastward and northward current components and the overbar representing a time average taken over a tidal cycle (Figure 4a) or over 5 min (Figure 4b). Away from the period affected by the storm the distribution of the vertical current shear over the whole deployment (Figure 4a) shows a general pattern of higher current shear near the surface and seabed. During the time of a well-defined semidiurnal signal in

the temperature time series (December 1 to December 6; Figure 2b) there was moderate shear in the interior of the water column. Focusing on the 5 min averaged shear over a single day in this period (Figure 4b) indicates that this internal shear was caused by the combined effect of the short-period internal waves (i.e., compare the patterns of shear and temperature variability in Figures 4b, and 4c).

The current profiles from the ADP on mooring IW4 can be used to provide estimates of the depth-integrated baroclinic kinetic energy associated with the dominant M_2 and inertial periodicities. The current vectors were first rotated 42° counterclockwise, aligning the y axis along shelf (positive to the northwest) and the x axis across shelf (positive to the northeast). The barotropic part of the current measurements was removed by subtracting the depth-averaged current from each profile. The resulting 1 min baroclinic current measurements were then used to provide hourly 10 min averages. Harmonic analysis was carried out on the baroclinic current time series at each level in the water column for periods of 12.42 and 20 hours. Noting that the beat frequency of the M_2 and inertial signals is about 33 hours, this analysis was conducted within a series of 36 hour windows, centered on each hour through the time series. For each 36 hour window the time-averaged vertical profile of baroclinic kinetic energy were then calculated for the two frequencies by

$$\text{KE}(z) = \frac{1}{2} \rho[u(z)^2 + v(z)^2] \qquad \text{J m}^{-3}, \tag{10}$$

with KE(z) the profile of either the M_2 or inertial kinetic energy and $u(z)^2$ and $v(z)^2$ the time-averaged square cross- and along-shelf components calculated from the results of the harmonic analysis. For the internal tide kinetic energy the time average was performed over one tidal cycle, while for the inertial kinetic energy the average was over one inertial period. The results (Figure 5) highlight three important points concerning the baroclinic variability. First, the internal tidal kinetic energy tended to be dominant, particularly during the period between December 1 and December 5 when the tidal signal was very clear (Figure 2b). Weak baroclinic inertial energy developed in response to wind events on November 26, November 28, and December 4. There is also an indication of
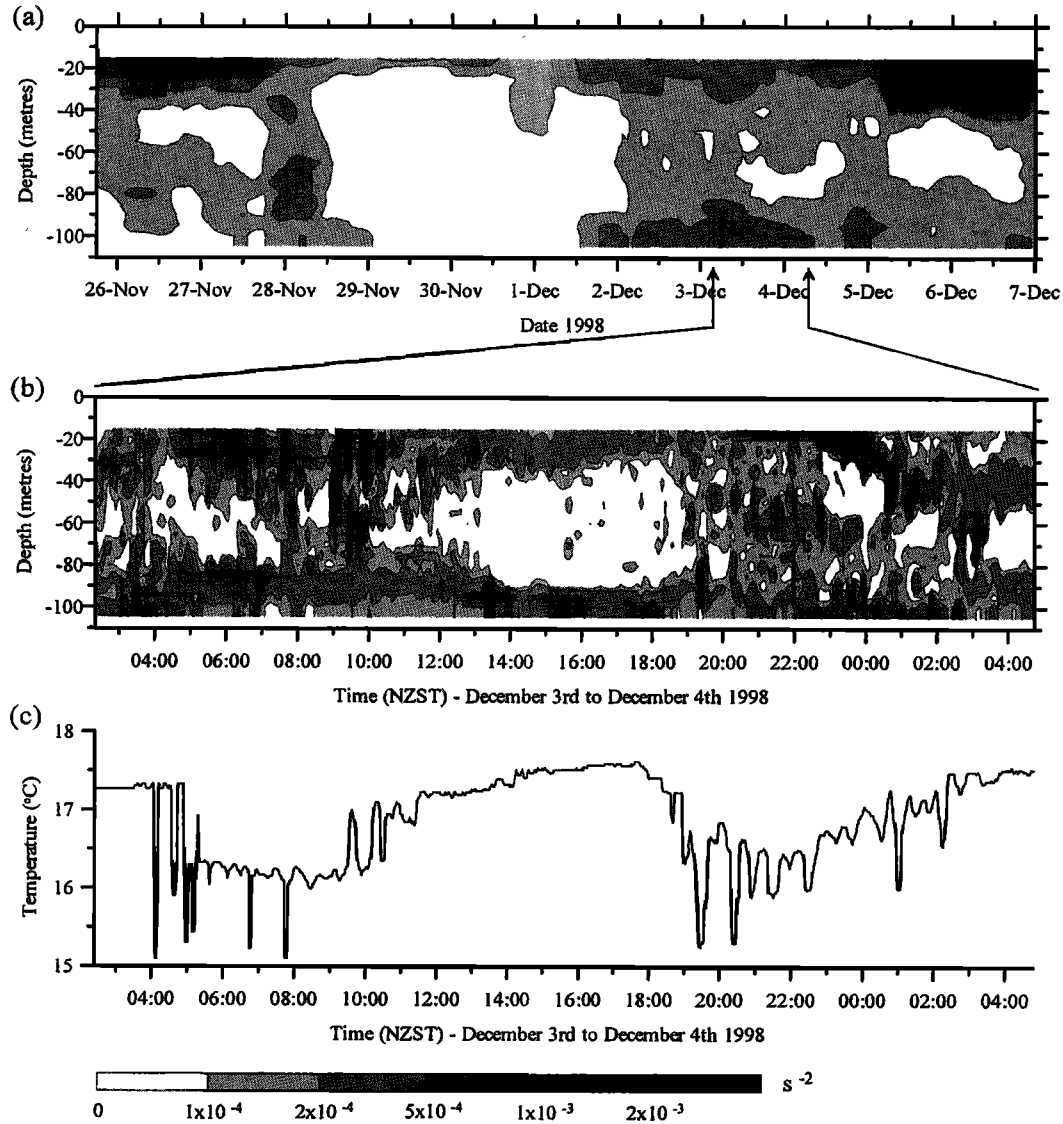
Figure 4. (a) Squared current shear from the ADP on mooring IW4 averaged over a one tidal cycle window for the entire deployment. (b) Squared current shear averaged every 5 min for the period 0200 hours on December 3 to 0500 hours on December 4. (c) Temperature time series from a depth of 70 m at IW4, over the same time as Figure 4b, illustrating the periods of internal wave activity within the internal tidal cycle.

weak baroclinic inertial energy following the storm, on December 1. Strong barotropic oscillations occurred during the storm (not shown). Second, the kinetic energy at both tidal and inertial periods tended to be greater nearer the surface and seabed boundaries. This is not surprising for the internal tide, but the reason for the existence of baroclinic inertial energy near the seabed is less obvious. The likely cause for this is the proximity of the coastal boundary forcing compensatory bottom layer flows in response to surface slopes set up by the surface inertial motions [e.g., *Rippeth et al.*, 2001]. Third, the kinetic energy associated with the internal tide reached farther into the interior of the water column than that associated with inertial oscillations.

The total energy in the internal tide is a sum of the kinetic and potential energies. As with the current data, the temperature data from both the IW2 and IW4 moorings was reduced to hourly 10 min averages. Harmonic analysis for the M_2 variability in the temperature time series was then performed

within the same 36 hour windows as the current analysis. A time series of vertical profiles of the tidally averaged potential energy of the internal tidal wave, PE(z), within each 36 hour window over the whole mooring deployment was calculated via

$$PE(z) = \frac{1}{4} N(z)^2 \rho(z) \eta_0(z)^2 \qquad \text{J m}^{-3}, \qquad (11)$$

with $N(z)$ (s^{-1}) the mean buoyancy frequency profile within the window and $\rho(z)$ (kg m^{-3}) the mean density profile. Here $\eta_0(z)$ (s^{-1}) is the vertical elevation amplitude of the internal tide (i.e., half the peak-trough range of the vertical oscillation) within each 36 hour window calculated by

$$\eta_0(z) = \frac{\Delta T_0}{\Delta T/\Delta z} \qquad \text{m}, \qquad (12)$$

with $\Delta T_0(z)$ the M_2 tidal amplitude of the temperature oscillation at height z found by harmonic analysis of the tempera-
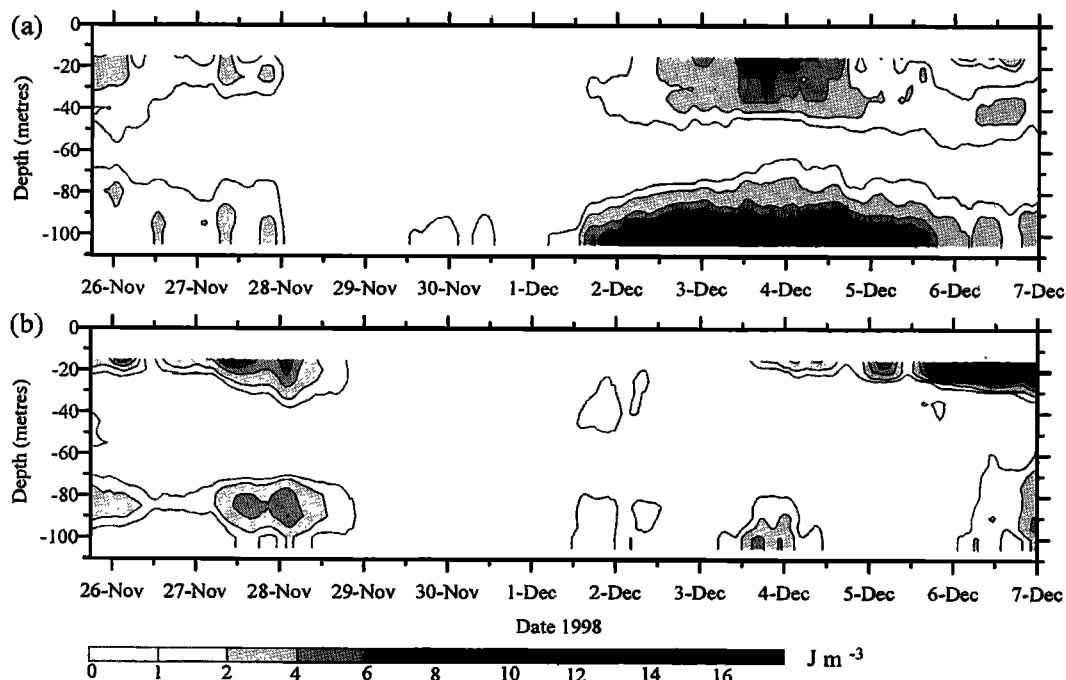
Figure 5. Vertical distribution of baroclinic kinetic energy at the (a) M_2 and (b) inertial frequencies, calculated from the results of the harmonic analysis. Values represent time averages over one tidal cycle in Figure 5a and over one inertial period in Figure 5b.

ture time series at each level in the water column and $\Delta T/\Delta z$ the local value of the vertical temperature gradient from the 36 hour averaged temperature profile.

Examples of the M_2 baroclinic current profiles and the vertical profiles of η_0 in the later, internal tide–dominated, part of the deployment (Figure 6) show typical internal tide behavior. Current amplitudes were maximum near the surface and bottom boundaries. The phase difference between surface and bottom current components was typically 180°, most of it occurring at middepth, indicating a dominantly first-mode internal wave. The vertical excursion of the density structure was maximum within the middle of the water column, with an almost depth uniform phase. Following Holloway [1994], the orientation of the internal tide current ellipse can be used to indicate the wave propagation direction, with the wave front lying normal to the direction of maximum currents (i.e., normal to the ellipse major axis). A time series of the depth mean ellipse orientation was calculated for the entire mooring deployment. Between December 1 and December 5 the average depth mean ellipse orientation was 7° (±16°) counterclockwise from the line through the mooring positions. Thus the tidal wave was propagating almost parallel to the orientation of the mooring array. The phases of the temperature variations were used to calculate the wave propagation speed between moorings IW1 and IW2 and between IW2 and IW4. The resulting mean wave speeds over the period December 1 to December 5 were 0.7 m s^{-1} between IW1 and IW2 and 0.4 m s^{-1} between IW2 and IW4.

The ADP provided current measurements between 9 mab and 11 m below the sea surface. Integration of the kinetic energy over the whole water column needs to take into account the increase in kinetic energy approaching the boundaries (Figure 4). To compensate for the lack of ADP data at the boundaries, the tidally averaged current components were ex-

trapolated on the basis of the local current gradients. Not taking account of this near-boundary kinetic energy leads to an underestimate of the total water column kinetic energy by about 20–25%. The depth-integrated tidally averaged energies at the two mooring sites (Figure 7) indicate that the baroclinic potential energies were typically about 200 J m^{-2} prior to the storm. Following the storm, the potential energy at IW4 was consistently lower than at IW2, typically by a factor of 2 or 3, but with a marked increase in potential energy at the shelf edge after December 6. The kinetic energy at IW4 was higher than the potential energy at the same site at times unaffected by the storm. Between November 27 and November 30 the potential energy at IW4 was greater than the kinetic energy. This difference appears to be linked to errors in the baroclinic current analysis near the surface at this time and is unlikely to be real. Calculation of $\overline{PE:KE}$ for site IW4 between December 1 and December 6 provides an average value of 0.5 ± 0.2. This value is not significantly different from the theoretical prediction of 0.46 (equation (1)). The total energy (PE + KE) at IW2 was always greater than that at IW4 (Figure 7b). The total energy at both sites was generally significantly larger than the energy at the inertial frequency. Two notable exceptions were the initial stages of the storm event, when the inertial energy was similar to the internal tidal energy at both mooring sites, and after about December 6, when the inertial energy exceeded the internal tide energy at IW4. At the end of the deployment the analysis shows a rapid increase in PE at IW2, without a corresponding increase at IW4. Without a continuation of the time series it is difficult to determine the cause of this, but it could be the result of a combination of rapid dissipation of a very large internal tide, and wave energy being reflected from the weaker shelf stratification.

The dissipation rate of the internal tidal wave can now be estimated for the period December 1 to December 5 by calculat-
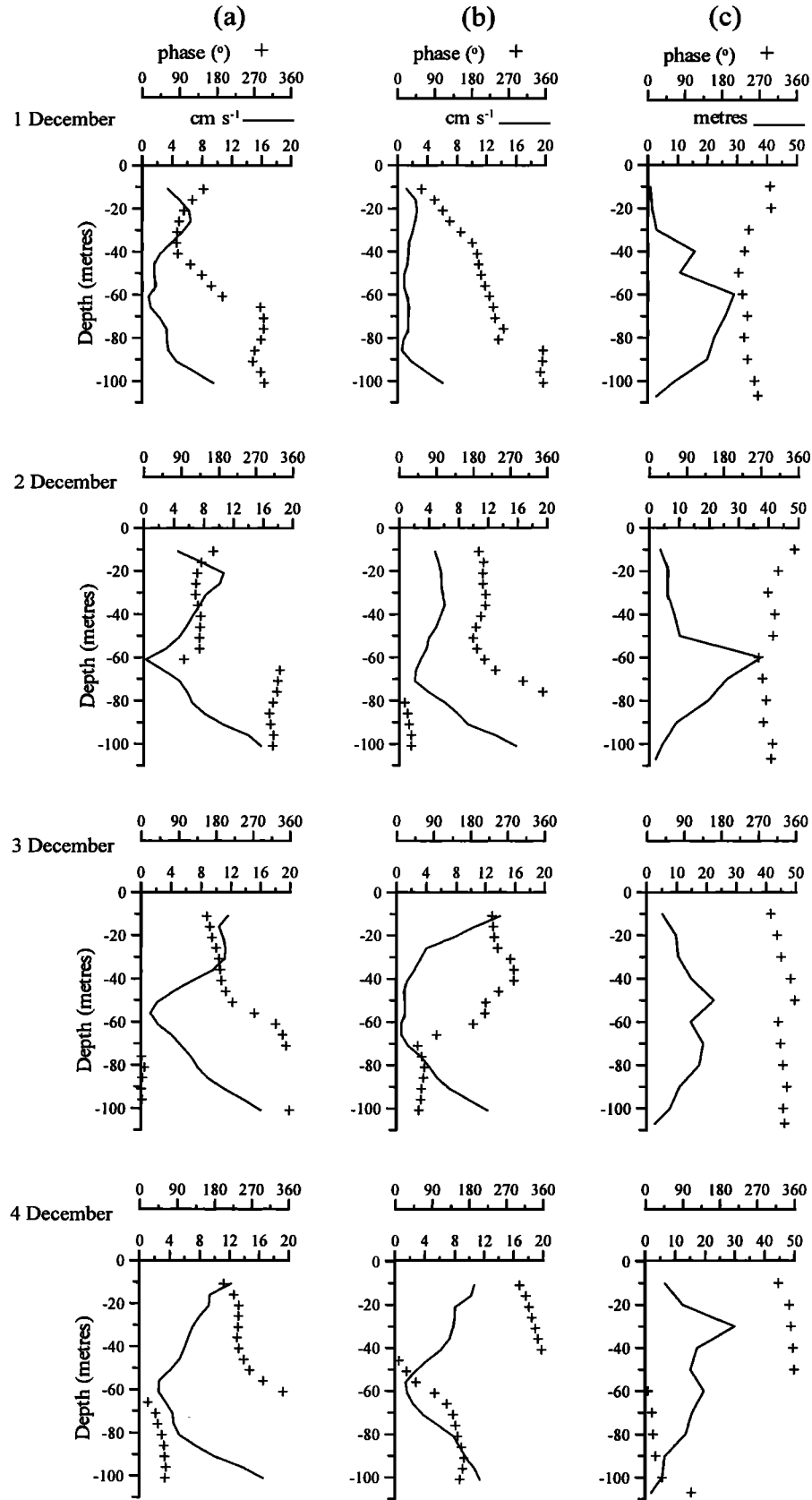
Figure 6. Examples of internal tide profiles from the harmonic analysis for December 1 to December 4: (a) cross-shelf baroclinic current amplitudes and phases, (b) along-shelf baroclonic current amplitudes and phases, and (c) amplitude and phase of the vertical elevation η_0.
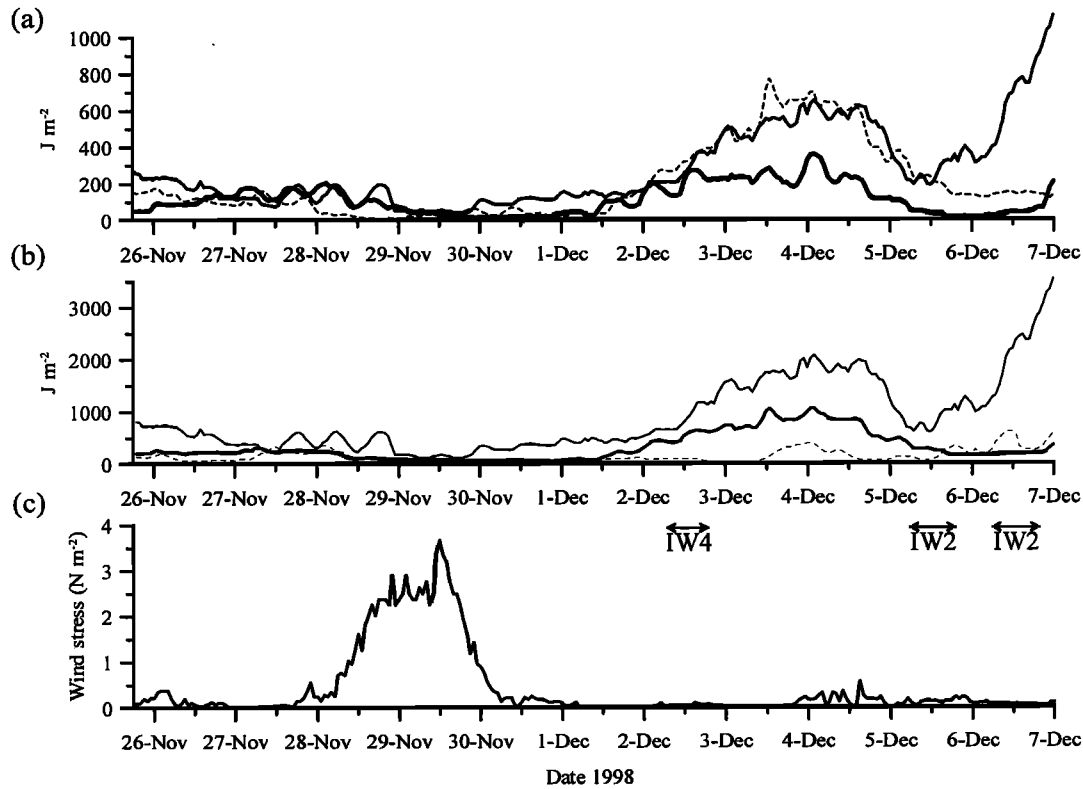
Figure 7. (a) Time series of the integrated water column potential energies of the internal tide at IW4 (bold line) and IW2 (thin line) and of the internal tide kinetic energy at IW4 (dashed line). (b) Integrated water column total internal tide energies at IW4 (bold line) and IW2 (thin line) and the integrated kinetic energy at the inertial frequency at IW4 (dashed line). (c) Wind stress. The horizontal arrows marked IW2 and IW4 below Figure 7b show the times at which microstructure profiles were carried out at the two moorings. Note that a microstructure station was also conducted at IW4 on December 7.

ing the change in total wave energy between the two mooring sites. The theoretical PE:KE ratio of 0.46 was used to estimate the KE of the wave at IW2. The resulting tidally averaged total wave energies at the two sites are estimated to be

$$IW4 \text{ total energy} = 480 \pm 340 \text{ J m}^{-2}$$

$$IW2 \text{ total energy} = 1100 \pm 700 \text{ J m}^{-2},$$

where the uncertainties in these calculations are dominated by the variability of the observed potential and kinetic energies during the mooring time series. Taking the mean depth between the moorings as 130 m and a wave propagation speed of 0.4 m s^{-1}, the mean energy dissipation rate between the two sites is calculated to have been $(1.1 \pm 0.8) \times 10^{-7}$ m^2 s^{-3} or $(1.5 \pm 1.0) \times 10^{-2}$ W m^{-2}. This should be regarded as a maximum dissipation rate as no attempt has been made to compensate for possible reflection of wave energy caused by the reduction in stratification between IW2 and IW4. Using (2) and a mean square buoyancy frequency in the latter part of the mooring deployment of 6×10^{-5} s^{-2} results in a mean value for the eddy diffusion coefficient of $K_\rho = (4 \pm 3) \times 10^{-4}$ m^2 s^{-1}. Taking a dissipation rate on the shelf of 10 mW m^{-2} and assuming a mean depth of 100 m and a mean internal wave propagation speed farther on the shelf of 0.3 m s^{-1}, the energy observed at IW4 should dissipate within about 16 km. Mooring IW4 was ~16 km from the coast, so it is reasonable to assume that reflection of wave energy at the coast will not be an important factor in the observations at IW2 and IW4.

3.2. Microstructure Observations

The microstructure data were segmented in 1 m vertical bins, between depth of 10 (to avoid contamination by the ship's wake) and 75 m. The data within each bin were used to provide a value of the dissipation rate ε (using (7)) and the eddy diffusivity K_T (from (5)). These results were averaged to provide 5 m values of ε and K_T. At each depth, ε and K_T were then averaged through time for each of the stations. The four stations, two at each of the mooring sites, thus provided tidally averaged profiles of turbulent dissipation and eddy diffusivity, with a vertical resolution of 5 m (Figure 8). There was little significant vertical structure in either ε or K_T during any of the stations, apart from a small reduction in K_T at depth on December 2 at IW4. A check on the consistency of the SCAMP measurements of ε and K_T was made by comparing K_T with $K\rho$ (using (2) and SCAMP's measurement of ε). The comparison was significant with 95% confidence ($r^2 = 0.44$ on the log-transformed data) with a mean Γ of 0.22.

All four stations were conducted when the baroclinic energies at the respective sites were dominated by the internal tide. For the stations on December 2, 5, and 6 this is clear from Figure 7b. For the station on December 7 the analysis based on the 36 hour windows does not allow a direct comparison of inertial and tidal energies at IW4, but the large internal tide amplitude during the station (Figure 2b) suggests that the internal tide was likely to be dominant. Apart from the internal tide and inertial oscillations, another potentially important
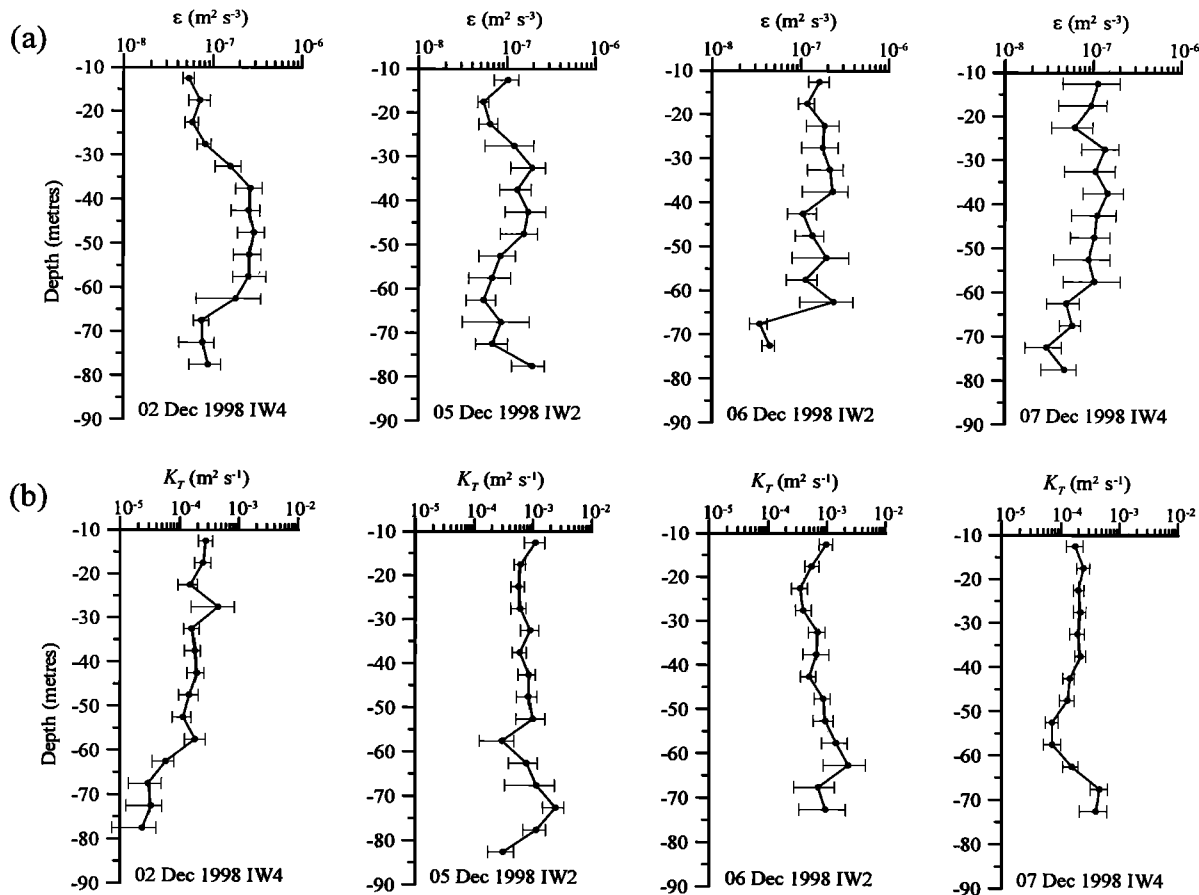
Figure 8. (a) Time-averaged vertical profiles of turbulent dissipation for each of the four microstructure stations. (b) Time-averaged vertical profiles of the vertical eddy diffusivity K_T for each of the four microstructure stations. Error bars mark the 95% confidence limits.

source of dissipation in the upper part of the water column is that driven from the surface boundary by wind stress. This is most likely at IW2 on December 5 and 6, when surface winds were about 5 m s^{-1}. The depth distribution of wind-driven dissipation can be estimated by $u_*^3/\kappa|z|$, with u_* the surface wind-driven friction velocity, $\kappa = 0.41$ the von Karman's constant, and z the depth. With a mean wind speed of 5 m s^{-1} this suggests dissipation rates of 1×10^{-7} m^2 s^{-3} at a depth of 20 m, decreasing to 5×10^{-8} m^2 s^{-3} at 50 m. Alternatively, the dissipation measured by SCAMP at a depth of 50 m was about 1×10^{-7} m^2 s^{-3}. The wind speed required to produce such a dissipation at that depth would have had to be in excess of 10 m s^{-1}. Thus, at IW2 it is likely that the dissipation observed in the upper 20 or 30 m contained a significant contribution from the wind, but deeper in the interior of the water column the dissipation was dominated by the internal tide. Considering the vertical distribution of shear in the water column (Figures 4a and 4b), the dissipation observed with SCAMP deeper than about 30 m was driven mainly by the short-period internal waves associated with the internal tidal wave.

4. Discussion and Conclusions

The estimates of total energy in the internal M$_2$ tide suggest a flux onto the shelf of 400 W m^{-1} in the latter part of the mooring deployment, though with significant intratidal variability. This flux is large compared to many existing observa-

tions (e.g., 70 W m^{-1} off Oregon [*Torgrimson and Hickey*, 1979] and 104 W m^{-1} on the Malin shelf [*Sherwin*, 1988]), though similar to the 300 W m^{-1} calculated for the NW Australian shelf [*Holloway*, 1984]. The high flux at the shelf edge of NE New Zealand is associated with an internal tide with a mid–water column peak-to-trough range of typically 40 m, reaching as much as 70 m, i.e., almost 50% of the total water depth.

The energy in the internal tidal wave was significantly larger than the energy at the inertial frequency through most of the mooring deployment. Estimates of the vertical profile of wind-driven dissipation during the weak winds experienced while making the microstructure measurements suggest that deeper than about 30 m, the wind stress was not making a significant contribution to the observed dissipation. Analysis for the barotropic tidal currents yielded a tidally averaged current speed of 5 cm s^{-1}, which implies a mean barotropic tidal dissipation rate of 0.4 mW m^{-2}. The evidence therefore suggests that away from the storm event, the dominant turbulent dissipation within the interior of the water column was driven by the passage of the internal tidal wave.

The passage of an intense storm through the region provided an opportunity to observe the complete breakdown, and subsequent recovery, of the internal tidal wave on the shelf. At the shelf edge the water column was homogenized down to ~70 m, leaving only a weak internal tide signal in the lower half of the
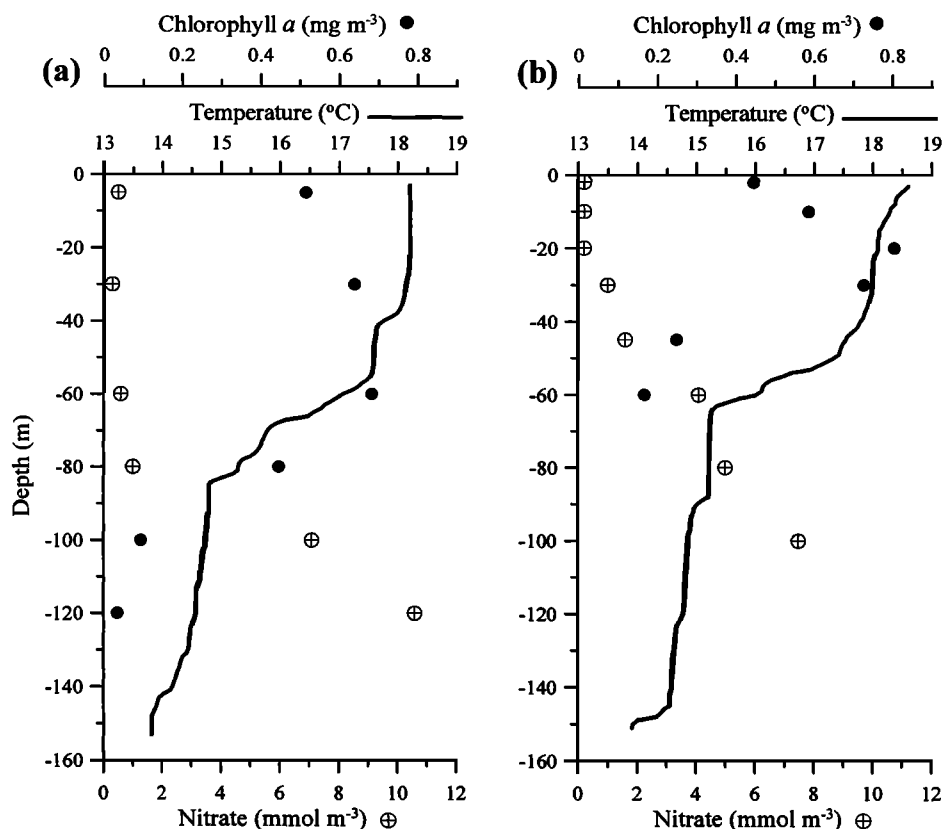
Figure 9. Examples of temperature, chlorophyll a, and nitrate profiles at IW2 on December 5 at (a) 0500 and (b) 1150 hours NZST.

water column. On the shelf the whole water column became mixed after about 24 hours of storm development, with a mean wind stress over that time of 0.7 N m^{-2} and a mean wind speed of 16 m s^{-1}. Over the entire storm event, between November 28 and November 30, the mean wind speed was 23 m s^{-1}. As the wind decreased, the internal tide rapidly returned at the shelf edge, with initial thermocline peak-to-trough oscillations with an amplitude of 20 m, gradually increasing to >70 m at the end of the mooring deployment. On the shelf, while surface stratification began to be reestablished following the reduction of the wind, the internal tide returned first near the seabed as dense water intruded onto the shelf. The appearance of this water is most likely driven by upwelling through the bottom boundary layer of the southeastward flowing East Auckland Current, which plays a key role in the cross-shelf fluxes in this region [*Sharples*, 1997]. The near-surface current meter on mooring IW1 recorded such along-shelf edge mean flows of about 10-15 cm s^{-1} during the latter half of the deployment.

The original motivation for this work was concerned with the diapycnal turbulent flux of nitrate into the photic zone driven by the internal tide. In this region of New Zealand the barotropic tidal mixing is so weak that in summer the water column becomes stably stratified and nitrate can become limiting in the surface water. The rate of diapycnal nitrate supply will therefore be an important factor in the control of new production in the subsurface biomass maximum and the surface water (Figure 9). The supply of nitrate from the deeper water is a combination of diapycnal mixing driven by the dissipation of the internal tide and episodic storm events that are strong enough to break down the near-surface stratification. The mooring and

microstructure observations allow us to assess the relative importance of these two processes to total shelf new production during summer.

The vertical nitrate flux driven by internal tide dissipation can be estimated by using the nitrate gradient observed with the bottle samples taken during the microstructure work (Figure 9), and the vertical diffusivity measured by SCAMP. The range of observations of the nitrate gradient at the base of the chlorophyll maximum was between 0.1 and 0.3 mmol m^{-4}. Using a mean diffusivity measured at IW2 within this gradient of ~7 × 10^{-4} m^2 s^{-1} implies a mean vertical nitrate flux of 12 mmol m^{-2} d^{-1}. Assuming that all of this nitrate is used for new production, and taking a C:N ratio of 6.6 for phytoplankton, suggests a potential new production rate of 1.2 g C m^{-2} d^{-1}. There are no available observations of production rates at the shelf edge in early summer, but midshelf and upper slope measurements of total net rates lie between 0.4 and 0.7 g C m^{-2} d^{-1} in late spring and 0.1 and 0.2 g C m^{-2} d^{-1} in late summer (J. Zeldis, personal communication, 2000). Over the summer period of 3 months we therefore estimate that the potential new production driven by the nitrate flux arising from internal tide mixing could be about 100 g C m^{-2}.

The effect that the storm had on the surface nitrate concentration at IW2 is well illustrated by the time series of nitrate concentration from the NAS2 analyzer on the mooring (Figure 10). Prior to and after the storm there was a clear internal tide signal in the nitrate time series, as the oscillation of the isotherms periodically allowed the analyzer to sample surface water (low nitrate, about 0.2-0.4 mmol m^{-3}) and deeper water (higher nitrate, ~1.0-1.2 mmol m^{-3}). The nitrate time series
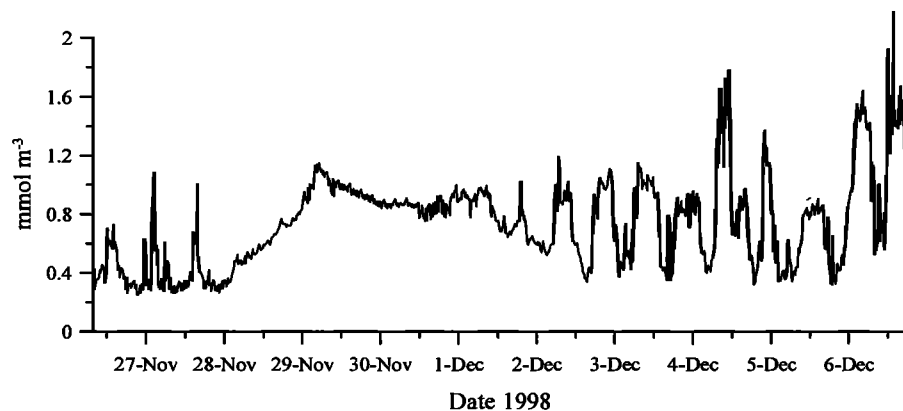
Figure 10. Time series of nitrate concentrations measured by the NAS2 analyzer 25 m below the surface on mooring IW2. The NAS2 was calibrated against discrete nitrate samples taken with the CTD.

through the storm indicates that the surface mixed layer reached a uniform concentration of about 1.0 mmol N m^{-3}. Thus the surface water received an additional 0.6–0.8 mmol m^{-3} as a result of the wind mixing. Taking a mean surface mixed layer depth, following restratification after the storm, of 30 m implies a supply of 18–24 mmol N m^{-2}. Again, using a C:N of 6.6, we can estimate that one such storm event could drive new production of between 1.5 and 2 g C m^{-2}. To estimate the number of these events in any summer, we assume that a daily mean wind speed of 15 m s^{-1} is sufficient to drive such a flux. Analysis of wind data from 1994 through to 1998 suggests that there are between 1 and 5 such events each summer between December 1 and March 1. Thus an estimate of the contribution to new production driven by these storm events is between 2 and 10 g C m^{-2} each summer, considerably less than that estimated for the internal tide mixing.

Less energetic wind events could also play a role in supplying nitrate to the surface water, with a combination of wind-driven turbulence and inertial shear acting to deepen the surface mixed layer temporarily. An estimate of this contribution to summer nitrate fluxes can be made by considering the change in the surface mixed layer depth in response to the wind impulse of the storm. Over 1.5 days (0000 hours November 28 to 1200 hours November 29) a mean wind stress of 1.8 N m^{-2} deepened the mixed layer at IW2 from 30 to 70 m (Figure 2a). Taking a mean summer mixed layer depth of $h_0 = 30$ m to represent a balance between surface heat supply and the median wind stress, deviations of the mixed layer depth, Δh, from h_0 can be estimated by

$$\Delta h = 15\tau_s \Delta t \quad \text{m}, \quad (13)$$

with τ_s the excess daily mean wind stress above the summer median value, $\Delta t = 1$ day, and the factor 15 (m (N m^{-2} d)$^{-1}$) linearly relates the deepening mixed layer to wind impulse. The original integrated mixed layer nitrate will be $N_{ML1} = N_0 h_0$ mmol m^{-2}, with $N_0 = 0.3$ mmol m^{-3} being the original surface mixed layer nitrate concentration. A deepening of Δh down through a linear nitrate gradient $\partial N/\partial z$ will result in a mean nitrate concentration within the layer Δh of $N_0 + 0.5\Delta h(\partial N/\partial z)$ mmol m^{-3}. Thus the integrated nitrate within the new surface mixed layer will be

$$N_{ML2} = N_0(h_0 + \Delta h) + \frac{\Delta h^2}{2}\frac{\partial N}{\partial z} \quad \text{mmol m}^{-2}. \quad (14)$$

Taking a value of $\partial N/\partial z = 0.3$ mmol m^{-4} from the CTD samples (Figure 9), the daily wind-driven nitrate flux was calculated for all the summer wind data between 1994 and 1998, only using the daily mean wind stress when it exceeded the median value, via

$$N_{flux} = \frac{N_{ML2} - N_{ML1}}{\Delta t} \quad \text{mmol m}^{-2}\,\text{d}^{-1}. \quad (15)$$

This very simple approximation ignores the potential for stronger stratification later in the summer inhibiting mixed layer deepening and assumes that the deep temperature and nitrate structure of the water column remains constant during summer. However, it does allow an order of magnitude estimate of wind-driven nitrate flux. Average fluxes calculated for all the available summer wind data ranged between 0.3 and 0.7 mmol m^{-2} d^{-1}, and so, a reasonable estimate for the average daily supply of nitrate to the surface mixed layer, driven by episodic wind variability, is taken to be 1 mmol m^{-2} d^{-1}. Using the Redfield C:N, this is sufficient to fuel a potential new production of about 8 g C m^{-2} over the whole summer, again, significantly less than that driven by the internal tide. Comparison with the estimate for strong wind events made earlier suggests, not surprisingly, that this wind-driven flux is dominated by storms.

It is worth noting one final piece of information provided by the nitrate sensor on the mooring at IW2 (Figure 10). Following relaxation of the winds on December 1 and the restratification of the surface water, the return of internal tidal oscillations allowed the sensor to sample periodically the surface water as the nitrate was being depleted. By December 3 the additional nitrate supplied by the storm had been removed to the background concentration. Furthermore, an estimate of the phytoplankton nitrate uptake rate of 8 mmol m^{-2} d^{-1} can be made by utilizing the rate of reduction of the surface water nitrate over the three tidal cycles between December 1 and December 3. This value is very approximate as the concentration of algae in the near-surface water would potentially be increasing in response to the development of stratification, but it does further indicate that the population was capable of utilizing the typical nitrate flux supplied by the internal tide.

Shelf regions where mixing is dominated by the barotropic tide have yielded estimates of cross-thermocline nitrate fluxes of around 2 [*Sharples et al.*, 2001] and 3–10 mmol m^{-2} d^{-1} [*Horne et al.*, 1996]. These fluxes are usually associated with

thermocline diffusivities at least an order of magnitude less than those calculated at the New Zealand shelf edge, but the existence of a bottom tidally mixed layer tends to aid the nitrate flux by sharpening the vertical nitrate gradient. By comparison, in the oligotrophic subtropical gyres, diapycnal nitrate fluxes tend to be at least an order of magnitude less than this [e.g., *Lewis et al.*, 1986; *Planas et al.*, 1999]. Our analysis has also suggested that off NE New Zealand, episodic wind-driven deepening of the surface mixed layer supplies bottom water nitrate to the photic zone at a rate one order of magnitude less than the internal tide. It is evident therefore that the baroclinically driven nitrate flux at the New Zealand shelf edge is an important process, comparable to, and potentially stronger than, cross-thermocline fluxes in shelf regions with strong barotropic tidal mixing. Tidal energy at the shelf edge and in shelf seas can be dissipated either directly by barotropic tidal stress on the seabed or indirectly by conversion of barotropic energy into the internal tide. By supplying nitrate the mixing associated with this dissipation clearly has the potential to drive important new production, both at the surface and within the subsurface water in stratified areas throughout summer. Primary production in stratified shelf seas is often thought of as being confined to the spring and autumn blooms, but annual production rates in these regions will also contain a large subsurface contribution of new production as a result of tidally driven diapycnal mixing.

References

Baines, P. G., On internal tide generation models, *Deep Sea Res., Part A, 29,* 307–338, 1982.

Efron, B., and G. Gong, A leisurely look at the bootstrap, the jackknife and cross-validation, *Am. Stat., 37,* 36–48, 1983.

Fofonoff, N. P., Spectral characteristics of internal waves in the ocean, *Deep Sea Res. Oceanogr. Abstr., 16, suppl.,* 59–71, 1969.

Garratt, J. R., Review of drag coefficients over oceans and continents, *Mon. Weather Rev., 105,* 915–929, 1977.

Gerkema, T., A unified model for the generation and fission of internal tides in a rotating ocean, *J. Mar. Res., 54,* 421–450, 1996.

Gregg, M. C., Estimation and geography of diapycnal mixing in the stratified ocean, in *Physical Processes in Lakes and Oceans, Coastal Estuarine Stud.,* vol. 54, edited by J. Imberger, pp. 305–338, AGU, Washington, D. C., 1998.

Holligan, P. M., R. D. Pingree, and G. T. Mardell, Oceanic solitons, nutrient pulses and phytoplankton growth, *Nature, 314,* 348–350, 1985.

Holloway, P. E., On the semidiurnal internal tide at a shelf break region on the Australian north west shelf, *J. Phys. Oceanogr., 14,* 1787–1799, 1984.

Holloway, P. E., Observations of internal tide propagation on the Australian north west shelf, *J. Phys. Oceanogr., 24,* 1706–1716, 1994.

Horne, E. P. W., J. W. Loder, C. E. Naimie, and N. S. Oakey, Turbulence dissipation rates and nitrate supply in the upper water column on Georges Bank, *Deep-Sea Res., II, 43,* 1683–1712, 1996.

Huthnance, J. M., Internal tides and waves near the continental shelf edge, *Geophys. Astrophys. Fluid, 48,* 81–106, 1989.

Imberger, J., and G. N. Ivey, On the nature of turbulence in a stratified fluid, part II, Application to lakes, *J. Phys. Oceanogr., 21,* 659–680, 1991.

Inall, M. E., T. P. Rippeth, and T. J. Sherwin, The impact of nonlinear waves on the dissipation of internal tidal energy at a shelf break, *J. Geophys. Res., 105,* 8687–8706, 2000.

Largier, J. L., The internal tide over the shelf inshore of Cape Point Valley, South Africa, *J. Geophys. Res., 99,* 10,023–10,034, 1994.

Ledwell, J. R., E. T. Montgomery, K. L. Polzin, L. C. St. Laurent, R. W. Schmitt, and J. M. Toole, Evidence for enhanced mixing over rough topography in the abyssal ocean, *Nature, 403,* 179–182, 2000.

Lewis, M. R., W. G. Harrison, N. S. Oakey, D. Hebert, and T. Platt, Vertical nitrate fluxes in the oligotrophic ocean, *Science, 234,* 870–873, 1986.

Moum, J. N., Efficiency of mixing in the main thermocline, *J. Geophys. Res., 101,* 12,057–12,069, 1996.

Munk, W., and C. Wunsch, Abyssal recipes II: Energetics of tidal and wind mixing, *Deep Sea Res., Part I, 45,* 1977–2010, 1998.

Oakey, N. S., Determination of the rate of dissipation of turbulent energy from simultaneous temperature and velocity shear microstructure measurements. *J. Phys. Oceanogr., 12,* 256–271, 1982.

Osborn, T. R., Estimates of the local rate of vertical diffusion from dissipation measurements, *J. Phys. Oceanogr., 10,* 83–89, 1980.

Osborn, T. R., and C. S. Cox, Oceanic finestructure, *Geophys. Fluid Dyn., 3,* 321–345, 1972.

Planas, D., S. Agusti, C. M. Duarte, T. C. Granata, and M. Merino, Nitrate uptake and diffusive nitrate supply in the Central Atlantic, *Limnol. Oceanogr., 44,* 116–126, 1999.

Rippeth, T. P., J. H. Simpson, R. J. Player, and M. Garcia, Current oscillations in the diurnal-inertial band on the Catalunyan shelf, *Cont. Shelf Res.,* in press, 2001.

Ruddick, B. R., A. Anis, and K. Thompson, Maximum likelihood spectral fitting: The Batchelor spectrum, *J. Atmos. Ocean. Tech., 17,* 1541–1555, 2000.

Sandstrom, H., and N. S. Oakey, Dissipation in internal tides and solitary waves, *J. Phys. Oceanogr., 25,* 604–614, 1995.

Sharples, J., Cross-shelf intrusion of subtropical water into the coastal zone of northeast New Zealand, *Cont. Shelf Res., 17,* 835–857, 1997.

Sharples, J., C. M. Moore, T. P. Rippeth, P. M. Holligan, D. J. Hydes, N. R. Fisher, and J. H. Simpson, Phytoplankton distribution and survival in the thermocline, *Limnol. Oceanogr., 46,* 486–496, 2001.

Sherwin, T. J., Analysis of an internal tide observed on the Malin Shelf, north of Ireland, *J. Phys. Oceanogr., 18,* 1035–1050, 1988.

Simpson, J. H., and D. Bowers, Models of stratification and frontal movement in shelf seas, *Deep Sea Res., Part A, 28,* 727–738, 1981.

Sjöberg, B., and A. Stigebrandt, Computations of the geographical distribution of the energy flux to mixing processes via internal tides and the associated vertical circulation in the ocean, *Deep Sea Res., Part A, 39,* 269–291, 1992.

Strickland, J. D. H. and T. R. Parsons, A practical handbook of Seawater Analysis, *Fish. Res. Board Can. Bull., 167,* 1–311, 1968.

Torgrimson, G. M., and B. M. Hickey, Barotropic and baroclinic tides over the continental slope and shelf off Oregon, *J. Phys. Oceanogr., 9,* 945–961, 1979.

E. R. Abraham, National Institute of Water and Atmospheric Research, Greta Point, Kilbirnie, Wellington, New Zealand.

C. M. Moore and J. Sharples, Southampton Oceanography Centre, Empress Dock, Southampton SO14 3ZH, England, UK. (j.sharples@soc.soton.ac.uk)